Adaptive electron beam shaping using a photoemission gun and spatial light modulator

Jared Maxson, Hyeri Lee, Adam C. Bartnik, Jacob Kiefer, and Ivan Bazarov
Cornell Laboratory for Accelerator-Based Sciences and Education, Cornell University, Ithaca, New York 14853, USA
(Received 9 October 2014; published 23 February 2015)

The need for precisely defined beam shapes in photoelectron sources has been well established. In this paper, we use a spatial light modulator and simple shaping algorithm to create arbitrary, detailed transverse laser shapes with high fidelity. We transmit this shaped laser to the photocathode of a high voltage dc gun. Using beam currents where space charge is negligible, and using an imaging solenoid and fluorescent viewscreen, we show that the resultant beam shape preserves these detailed features with similar fidelity. Next, instead of transmitting a shaped laser profile, we use an active feedback on the unshaped electron beam image to create equally accurate and detailed shapes. We demonstrate that this electron beam feedback has the added advantage of correcting for electron optical aberrations, yielding shapes without skew. The method may serve to provide precisely defined electron beams for low current target experiments, space-charge dominated beam commissioning, as well as for online adaptive correction of photocathode quantum efficiency degradation.

DOI: 10.1103/PhysRevSTAB.18.023401 PACS numbers: 07.77.Ka, 42.79.Kr

I. INTRODUCTION

For any photoemitted electron beam, the 3D intensity distribution of the laser determines the initial density distribution of the electrons. The 3D distribution has been shown to have a significant impact on the emittance evolution of a space charge dominated beam [1–5], and is significant for various other applications such as conventional or cold atom electron sources for electron diffraction [6,7], or next generation acceleration techniques [8,9]. Furthermore, during high current photoinjector beam operation, the uniformity of the photocathode can be damaged by various phenomena including ion back-bombardment, high voltage discharge, or increased vacuum pressure, and may therefore change the electron density from a given laser shape as a function of time. Ion back-bombardment in particular will cause a spatially dependent decrease in photocathode quantum efficiency (QE), or the electron yield per incident photon [10]. Thus, precise shaping of the transverse dimensions for beam dynamics purposes should ideally also be adaptive to account for changes in QE.

With a few notable exceptions ([11], [7], and [12]), the transverse Gaussian output of drive lasers is most often shaped to a semi-flattop shape via truncation with a pinhole, and subsequent imaging of this pinhole onto the cathode. The notable exceptions include [11], which used a deformable mirror as an adaptive transverse shaper. With the use of a genetic algorithm to search for the mirror shape, a much improved semiflat beam output was achieved. In [7] and [12], a spatial light modulator (SLM) was used with a modified Gerchberg-Saxton (GS) iterative Fourier transform method, e.g. [13–15], to make arbitrary beam shapes from a cold atom gas. However, in these cases, the beam profile is modulated by the density of the gas cloud, which alters the beam shape. Here again, an adaptive method which accounts for the spatially varying yield of electrons could be of use.

In this paper we demonstrate that using a commercially available liquid crystal spatial light modulator (Hamamatsu LCOS-SLM X10468-04) in the transverse plane to shape a drive laser, a low current beam from high voltage dc gun imaged onto a target plane can be shaped with high accuracy. Instead of computationally intensive iterative Fourier transform methods, we use a much simpler method of SLM-based polarization masking [16,17], described in detail below. This method has been shown in [18] to have nearly equivalent performance in terms of accuracy and efficiency to the best Fourier space method. We demonstrate that this method has both the ability to offer a precise transverse shape for beam dynamics purposes, but also the adaptive capability to correct for imperfections in the quantum efficiency of a photocathode. Furthermore, we show that using a calibration to match the coordinates of the SLM with the coordinates of the target plane, the low-current target image can be shaped to undo any effects of electron optical aberrations.

Prior to using a SLM, we tested a variety of methods to shape our laser beam, but eventually found each to be unsatisfactory. We will describe each briefly here, so as to

guide practitioners in the field. We tested a refractive beam shaper (Newport GBS-AR14), which takes in a Gaussian beam and produces a flattop profile. This shaper worked very well when supplied with a good quality Gaussian beam with a precise initial size and divergence, but it was not realistic to use this in practice with our nonideal input beam, and more importantly it does not allow for a tunable shape. See also [19]. Similarly, we also tested an engineered diffuser (Thorlabs ED1-C20) which produces a uniform flattop speckle pattern for an arbitrary input beam. Because it produces the same output for almost any input, this is practically very attractive, but it suffers from too large of a beam divergence after the optic. Thorlabs was able to custom order smaller divergences, at the loss of some output beam quality, but not sufficiently small for our in-vacuum beam transport to the cathode. Furthermore, clearly this would not provide any adaptive capability. But, for applications with a fixed desired shape with a smaller beam transport a custom ordered diffuser would be a very attractive option. Also, others have demonstrated light shaping using digital micromirror devices for beam instrumentation [20,21]. Apart from SLMs, micromirror devices may offer another option for high accuracy [22] drive laser shaping.

The SLM method requires a single linear polarization of all input light. However, in the case of birefringent crystal temporal shaping there are multiple polarizations in the input pulse train [23]. Nevertheless, we found producing one linear polarization after this temporal shaping to not be a problem in practice when only moderate overlap of the differently polarized pulses is employed. An example of such an overlap is shown in [24]. A linear polarizer rotated at 45° to the optic axis of the birefringent crystals will produce linearly polarized light at the expense of 50% intensity reduction.

Liquid crystal SLMs have a damage threshold given by the onset of thermal effects. For pulsed lasers, the damage threshold of such SLMs is a function of both peak and average power, and is generally not yet well studied. The vendor of our SLM has shown this model to withstand at least 2.6 W/cm^2 average power (with 101 MW/cm^2 peak power) without damage when illuminated with a 515 nm pulsed laser for 8 hours [25]. While not exhaustive, these data suggest that current SLMs may be applicable to a wide array of photoinjectors.

In principle, a shaping method such as demonstrated in [11] using a deformable mirror, would not be sensitive to the polarization and may have a higher damage threshold. We attempted to use a deformable mirror (Okotech, 37 Channel, 15 mm) to achieve a tunable beam profile. Contrary to [11], we found that the limited number of actuators in the mirror prevented us from having the necessary flexibility to go from an arbitrary and nonideal initial distribution to a desired output. More details about the deformable mirror are given in the Appendix.

The organization of the paper is as follows. We will first give an overview of the SLM-based high accuracy polarization-mask shaping method which was introduced in [17], first implemented in [16], and characterized in terms of efficiency in [18]. In this paper we describe its implementation with an actual photogun [26]. We will then show that the transmission of the shaped drive laser to the cathode results in an electron beam shape of similar fidelity. Finally, we will show that using an active feedback with an unshaped beam, we can achieve similarly high fidelity beam shapes free from electron optical aberrations and QE nonuniformities present in our system.

II. POLARIZATION-SUBTRACTIVE SLM TRANSVERSE LASER SHAPING

A diagram of the setup is shown in Fig. 1. The liquid crystal orientation rotates in the x-z plane as a function of the SLM setpoint, where z is the direction of propagation of the incident light. The orientation of the liquid crystal can vary from pixel to pixel. Thus, the SLM can apply a spatially varying phase to light polarized in the x direction. Each pixel is capable of applying a phase $\Phi_{ij} \in [0, 2\pi]$ to the incident light, where i and j are pixel indices. One can then compute phase profiles that shape the light in a refractive [27] or diffractive manner [28]. The best diffractive methods, variants of the GS holographic method, are lossy [15,29]. For simple shapes, these losses are comparable to the method described below [18], which is computationally simpler.

With two passes through a quarter-wave plate aligned at 45° to the initial polarization, as in Fig. 1, the spatially dependent phase delay of the SLM is converted into a linear polarization rotation [16,17]. Each pixel will rotate the

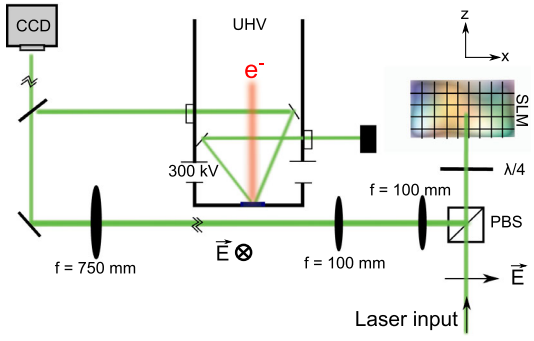

FIG. 1. 532 nm diode laser light enters from the bottom along z and is polarized along x. A quarter-wave plate and SLM act as a polarization rotator with spatial dependence, which shapes the light when used with a polarizing beam splitter (PBS). The surface of the SLM is then 4-f imaged onto an intermediate plane to preserve the beam divergence, and then this intermediate plane is imaged with a single long focal length lens onto either the photocathode or a CCD. An ultrahigh vacuum (UHV) mirror reflects light to the center of the photocathode. A dc bias of 300 kV accelerates the photoemitted electrons.

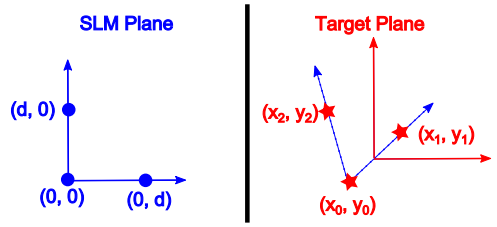

FIG. 2. Coordinate systems of both the SLM and target planes, showing a possible skew transformation between the two.

phase of the incident light by $\theta_{ij} = \Phi_{ij}/2$. A polarizing beam cube is set to reflect light polarized perpendicular to the initial polarization. Thus, applying a phase of $\Phi_{ij} = \pi$ on a particular pixel will transmit all light incident on that pixel to the CCD or cathode. The intensity of the transmitted light is theoretically zero at a applied phase of zero. In real application, phase error in the SLM, imperfect polarization control of the input light, and spurious reflections from the beam cube may contribute to a nonzero background intensity in the target plane. The smallest spatial scale that can be modulated is set by the size of the SLM pixel, which is 20 μm in our case. In general, we refer to this method as the polarization subtractive method, as the laser is shaped by the spatially varying masking of the initial unshaped intensity. The efficiency of the method as compared to other SLM based laser shaping methods was studied in [18]. As such, our discussion of the efficiency in this paper will be limited.

To create an arbitrary laser shape, one must first establish the relationship between the coordinate system of the SLM and the target plane given by the properties of the optical transport from one to the other. This is done by setting the phase of individual SLM pixels to maximum transmission $\Phi = \pi$ and measuring the position of the resultant intensity maximum in the target plane, as shown in Fig. 2. In the case of preshaping the laser before transmission to the cathode, the target plane is the CCD. We account for a linear skew transformation between the SLM coordinates and the target plane, rather than simply rotation and magnification, anticipating that this method might accommodate various other linear optical aberrations between the SLM and target planes. We transmit light from only three pixels on the SLM, forming a right triangle: (0, 0), at the geometric center of the SLM, and two points a distance d from the center. The position of the three points in the target plane we denote by (x_0, y_0), (x_1, y_1) and (x_2, y_2). From these points we can determine the general linear transformation that takes any point on the SLM $(x_{\mathrm{SLM}}, y_{\mathrm{SLM}})$ to the corresponding point in the target plane (x_T, y_T), assuming only that the transformation is linear:

$$\begin{pmatrix} x_T \\ y_T \end{pmatrix} = \begin{pmatrix} x_1 & x_2 \\ y_1 & y_2 \end{pmatrix} \begin{pmatrix} x_{\mathrm{SLM}} \\ y_{\mathrm{SLM}} \end{pmatrix} \frac{1}{d} + \begin{pmatrix} x_0 \\ y_0 \end{pmatrix}. \quad (1)$$

Once this transformation is established, we generate an arbitrary target laser intensity distribution, defined in the target plane coordinates. Then we apply the inverse of the transformation in Eq. (1) to generate the required target in the SLM plane. This ensures that the target plane output will be upright and skew free.

We then apply a uniform phase of π to the SLM, transmitting all light to the CCD, which measures the initial intensity distribution denoted by U, from which we will subtract. This image is transformed to SLM coordinates via the above scheme, and the phase applied to the SLM is given by

$$\Phi_{ij} = 2\sin^{-1}\left(\sqrt{\frac{\alpha T_{ij}}{U_{ij}}}\right), \quad (2)$$

where T is the target, and α is a numerical scaling factor for the target. For maximum theoretical accuracy and efficiency, alpha should be set to

$$\alpha = \max\left(\frac{T'_{ij}}{U'_{ij}}\right), \quad (3)$$

where the prime denotes that the distribution should only be evaluated where the *target* is nonzero. This value is such that the theoretical efficiency is maximum while keeping the target intensity αT less than the initial intensity U at all points.

A practical limitation of the method is the presence of multiple reflections from the PBS and nearby mirrors which can overlap the intensity distribution, causing a small quantity of unmodulated light to leak through to the target plane, even with a setting of zero transmission. We found this leakage light to be present even with precise polarization alignment, and clipping of all visible spurious reflections. This leakage light was measured to be 2% of the total intensity when the phase was set uniformly to zero transmission. This leakage distribution does not change significantly with phase modulation, and thus its inclusion in U is erroneous, and makes the output in the target plane given by Eqs. (2) and (3) to be slightly incorrect.

To correct for this, we apply an active feedback to reduce the error of the output distribution. The first guess output, which we now denote with an extra iteration superscript I^0_{ij}, is used to change the first guess phase Φ^0_{ij}. First, α^0 is recomputed:

$$\alpha^\gamma = \max\left(\frac{\tilde{T}_{ij}}{\tilde{I}^{\gamma-1}_{ij}}\right), \quad (4)$$

where γ is the feedback iteration index, and the tilde means evaluating the distributions at only those pixels where $\Phi_{ij} = \pi$, or where the transmission is maximum. Thus, the maximum in Eq. (4) finds the worst case pixel for which the transmission is maximum but the output is maximally far from the target. All images below, unless stated otherwise,

are median filtered, so as to reduce any influence of dead pixels on this definition of α.

The phase during feedback is then adjusted according to

$$\Phi_{ij}^{\gamma} = \Phi_{ij}^{\gamma-1} + \epsilon(\alpha^{\gamma} T_{ij} - I_{ij}^{\gamma-1}). \tag{5}$$

Here ϵ is a constant that both converts intensity units to phase, as well as ensures that the relative adjustment between iterations is small. Note that we do not again employ Eq. (2), which would depend on the initial image. Here, we simply exploit the fact that output is very near the target, and that a pixel's transmission is a monotonic function of phase, when the bounds are enforced to be $[0, \pi]$. With an intensity scale normalized to unity, we found sufficient convergence with $\epsilon = 0.05$ radians.

Beam output in the target plane is quantitatively compared to the target in terms of the root-mean-squared (rms) error, which is defined as

$$\text{rms error} = \left[\frac{1}{N}\sum_{ij}\left(\frac{\beta I'_{ij} - T'_{ij}}{T'_{ij}}\right)^2\right]^{1/2}, \tag{6}$$

where N is the number of pixels inside the nonzero target region, and β scales the actual intensity I such that the rms error is minimal. Note that any intensity of I outside of the target region is not included in the calculation of the error. We will discuss background minimization outside of the context of rms error.

Our first target of choice was a hard edged flattop circle of diameter $D = 2$ mm as measured in the target plane. The initial laser beam before shaping, the first feedback guess, and shape after seven iterations of feedback is shown in Fig. 3. If α is defined as above, feedback proceeds by removing additional light from the distribution. In the case of Fig. 3, feedback was stopped when the rms error of the flattop reached 10%, so as to maintain good efficiency. The efficiency as estimated by both CCD images was 16%. Unmodulated leakage light is visible in Fig. 3(c), in which the shaped power is the smallest. Flattops with even higher degrees of flatness using this method can be seen in [18].

III. TRANSMISSION OF SHAPED LASER LIGHT TO THE PHOTOCATHODE

The method by which laser light is introduced to the gun vacuum chamber, and the electron imaging beam line is shown in Fig. 4. Light is transported to the gun via a vacuum window and an in-vacuum mirror in a dedicated laser entrance chamber (not shown). The in-vacuum mirror directs the laser toward the center of the photocathode, and a second in-vacuum mirror directs beam reflected off the photocathode out of the vacuum chamber to a beam block. The photogun used has been described in detail elsewhere [26]. A Cs_3Sb cathode with average QE of 6% at 532 nm was used.

The electron beam was emitted with average (across all shapes produced) current density of approximately 30 nA/cm^2 at the photocathode, and thus the space charge force is negligible here. The beam is accelerated to 300 kV using a cathode-anode gap of 50 mm. A solenoid magnet 38 cm downstream of the photocathode is used as an imaging electron lens to image the cathode surface on to the 1.5″ diameter BeO fluorescent viewscreen, angled at 45° to the beam direction. The solenoid field profile is shown in Fig. 4. The fluorescence from the BeO prompted by the electron beam was imaged by a lens and CCD. We assume this fluorescence distribution to be directly proportional to the beam transverse distribution. We will slightly modify this assumption later. The size of the image taken with the CCD was calibrated via landmarks on the in-vacuum BeO holder, a method which is accurate to 5%, when compared to beam deflections from corrector magnets with known magnetic fields. The imaging solenoid field setting was found to correspond to particle tracking simulations to ±2%. At these settings, the photocathode plane is magnified by a factor of 3.8 on the viewscreen, and the photocathode image is rotated by a Larmor angle of 46°.

The laser profile shown in Fig. 3(c) was transported to the cathode according to the above scheme, and the resultant beam profile measured on the viewscreen is shown in Fig. 5(a). There are several features to note. The first is that the flatness of the laser shape is preserved in the electron beam, further indicated by the line cuts in

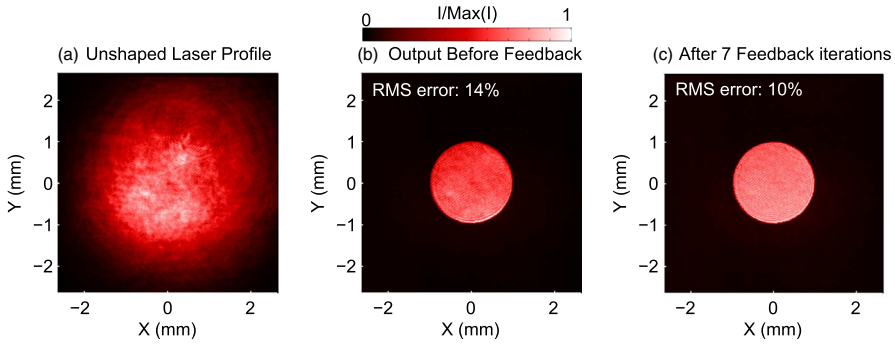

FIG. 3. (a) The initial near-Gaussian unshaped laser profile, U. (b) Shaped profile, a 2 mm diameter flattop, prior to feedback, I^0. (c) After seven feedback iterations, the rms error is reduced to 10%. Each image is scaled to its respective maximum.

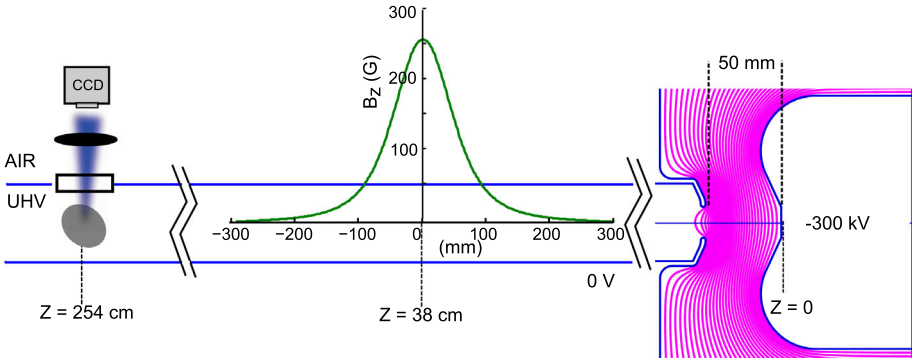

FIG. 4. Layout of the electron beam line, including the photogun (purple equipotential lines), imaging solenoid, and BeO fluorescent viewscreen and fluorescence profiling camera.

Fig. 5(c), from which we calculate a variation of only 4% rms. The second feature is a ring of decreased intensity around the shape. This fluorescence is not directly modulatable with laser power; changing the SLM transmission at the flattop edge changes only the fluorescence on the edge of the bright interior. We believe this edge effect to be due to diffuse scattered beam fluorescence from the BeO, and does not correspond to a spatial "tail" in the electron distribution. This was further verified by clipping the electron beam with an aperture upstream of the screen, in which this tail effect was also seen.

Next, it is clear that the beam is no longer round. As the beam is round on an upstream viewscreen (not shown, $Z = 130$ cm), this is not due to poor laser transport. We believe this is due to both imperfect alignment in the solenoid and a stray quadrupole magnetic field in the beam line. Though this can obviously be remedied with more perfect alignment and reduction of unwanted fields, we will correct for this electron optical aberration in the next section by using the SLM.

Finally, we note that the leakage light described above is also visible in the electron beam profile in Figs. 5(a) and 5(d). However, placing an appropriately sized pinhole in the imaging plane of the second lens downstream of the SLM can clip this leakage light without altering the central shape, as demonstrated in Figs. 6(b), 6(c), and 6(e).

To illustrate the shaping capability of the SLM, we chose a much more elaborate laser target with various intensities

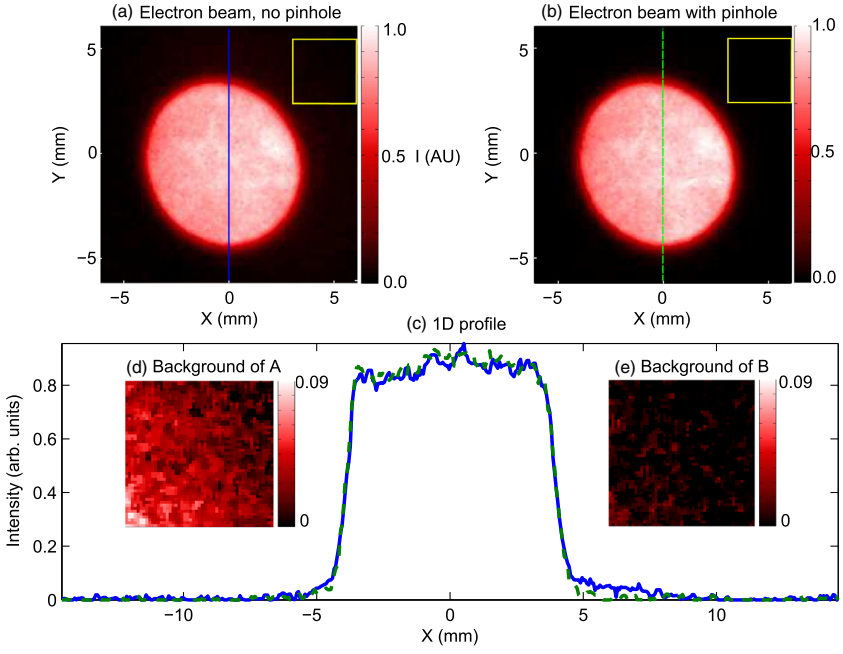

FIG. 5. (a) Resultant beam profile when the flattop shown in Fig. 3(c) is transported to the cathode and the beam imaged on the viewscreen. (b) Beam result when a pinhole is placed in the image plane of the second lens downstream of the SLM. (c) 1D profiles along the lines shown in (a) and (b). (d) Background of (a), taken from yellow boxed region. (e) Background of (b), taken from the yellow boxed region.

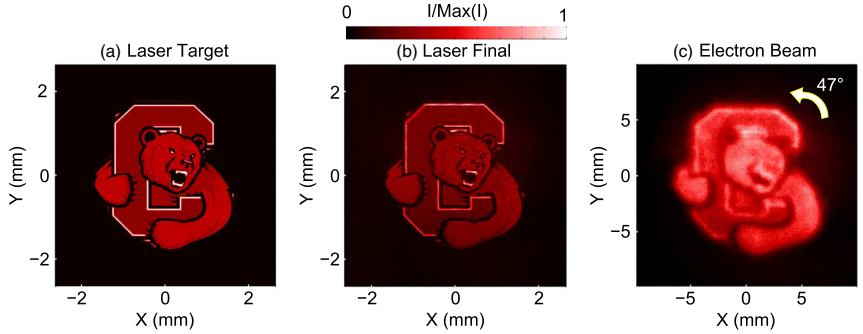

FIG. 6. (a) Laser target (see text for details). (b) Final measured laser distribution. (c) Resultant beam distribution, rotated by 47 degrees in after acquisition, with no median filter.

and feature sizes. The Cornell University bear logo [30] was used, converted to gray scale, as shown in Fig. 6(a). The laser profile output of the laser shaping as described above is shown in Fig. 6(b), which illustrates that polarization subtractive shaping is capable of resolving fine detail in both shape and intensity. To get an estimate of the error of this output image, the target was thresholded at 15% of its maximum value to remove small intensity points from inclusion in Eq. (6), which yields an rms error of 20%. The efficiency was estimated from the CCD images of the initial beam and the final output to be 8%.

This shaped light was then transmitted to the cathode and the resultant beam was imaged onto the viewscreen, giving the distribution shown in Fig. 6(c). The image is not median filtered, but is rotated to remove the Larmor angle. While the image still suffers the same aberrations in Fig. 5 and the smallest details are lost, most fine features are preserved.

IV. ACTIVE ELECTRON BEAM FEEDBACK

Instead of transmitting a shaped beam profile to the cathode, we can instead transmit the unshaped laser beam and perform shaping on the electron beam image formed on the viewscreen. This method has two clear advantages. First, the laser profile is never directly imaged; only the product of the laser distribution and the QE distribution is known. Thus, this method will automatically correct for any QE nonuniformities. Second, with the electron viewscreen as the target plane, the above calibration with full skew transformation will also correct for any electron optical aberrations.

The coordinate transformation scheme described above in Fig. 2 is used with only slight modification. The target coordinates are those of the CCD which images the beam induced fluorescence. Instead of illuminating one pixel per triangle side, we illuminate three 3×3 square groups of pixels on the SLM, with each square centered on the points of the right triangle in Fig. 2. The resultant electron beam intensity maximum is then chosen as the corresponding point in the target plane.

This calibration scheme was found to systematically overestimate the size of the target area by a small amount. When lined up with the output on the viewscreen, the target shape only just encloses the nonmodulatable tail presumed to be from diffuse scatter described above. This leads to the generation of artifacts in the beam shape. To improve the coordinate system agreement, the target coordinates were reduced by 5% when compared to the output image, which is the minimum adjustment that keeps the nonmodulated tail outside of the shaping region. This coordinate matching was aided by a 10×10 pixel average filter applied to the image for use in feedback (though not for error computation).

With these changes to the beam shaping feedback, we first chose to make a flattop of comparable size to that of Fig. 5. The initial unshaped beam, the final feedback output, and the error as a function of feedback iteration are shown in Fig. 7. At the feedback error minimum, the beam distribution has flatness nearly equal (4%–5%, depending on the position) to that shown of Fig. 3. The rms error of the whole shape, which includes any mismatch between the target and output, is smaller than the error in the laser shape of Fig. 5, and is thus also very round. This indicates that the calibration scheme can successfully remove effects of electron optical aberrations. After reaching a minimum of error, further iterations usually increase the error, as seen in 7. This is due to small misalignment between the target and SLM plane coordinates. This mismatch causes an erroneous overcorrection in subsequent iterations. In practical application, this overcorrection can be detected and suppressed. After feedback, with a constant SLM setpoint, we did not observe any time dependent image quality degradation.

Though this method automatically corrects for any spatial QE dependence, as only the product of the laser intensity distribution and the QE distribution is ever measured, our results with the transmission of shaped laser to the photocathode indicate that there was no significant QE slope in the illuminated photocathode area. We emphasize the QE corrective capability of the method by creating a flattop shape via beam feedback with an additional small bump, which simulates an area of low QE for which more laser power would be desired. This electron beam feedback

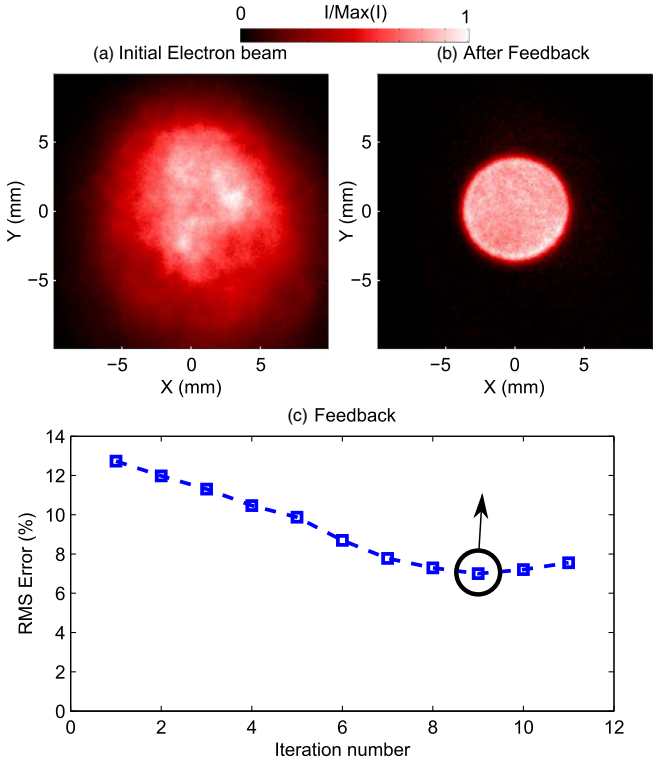

FIG. 7. (a) Initial unshaped electron beam imaged on the fluorescent screen. (b) Final output of electron beam-based feedback, with no profiling of the drive laser. (c) Progress of feedback versus iteration. The distribution shown in (b) is circled.

shape is shown in Fig. 8. Furthermore, the truncated Gaussian, another electron profile of interest for beam applications [31], is also shown Fig. 8. Both shapes have an rms error $< 10\%$.

To test the ability of the electron beam feedback method to resolve small features, we chose to create the target of Fig. 6. In this example, we omit the 10×10 pixel average filter, to maximize resolution. With the inclusion of the skew transformation, the electron shape should be upright

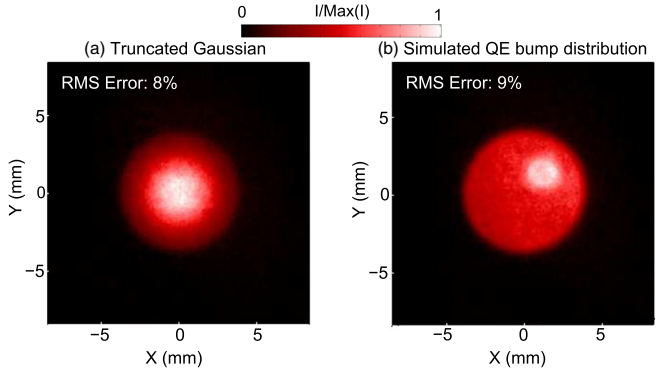

FIG. 8. (a) Electron beam distribution created with beam feedback: A truncated Gaussian. (b) A beam shape for a hypothetical photocathode with a local QE dip, thus requiring a local maximum on the laser power (electron beam shown).

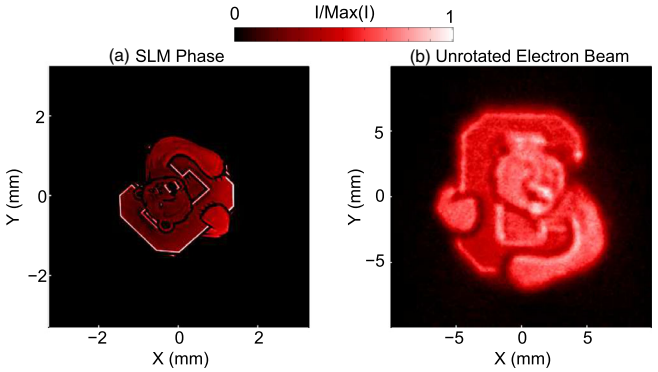

FIG. 9. (a) Phase applied to the SLM to create the shape in (b). The phase ranges from $[0, \pi]$. (b) Electron beam distribution created with electron beam feedback, which does not directly profile the laser. The target distribution is that of Fig. 6(a), scaled by the electron magnification.

in the target plane coordinates. The results of beam feedback are shown in Fig. 9. The target is indeed upright, and the rotation and skew are now placed in the SLM plane shape, also shown in Fig. 9. We find comparable fidelity to the shape shown in Fig. 6(c). This suggests that traditional laser shaping prior to transmission to the gun could instead be performed by beam feedback at low current without loss of electron beam quality.

V. CONCLUSIONS AND OUTLOOK

In this paper, we show that a simple method of SLM-based laser shaping, the polarization subtractive method, enables us to generate arbitrary to generate arbitrary low-current electron beam shapes of high accuracy from photoelectron sources. We demonstrate that the most direct beam shaping method of transporting a preshaped laser distribution to the cathode can preserve many of the features of the electron beam distribution, but will also naturally suffer from the electron optical aberrations. We demonstrate that these electron aberrations can be corrected using a feedback method at a target plane, using a simple calibration scheme. This method has the added benefit of never directly imaging the laser profile, and thus the feedback will correct both laser distribution irregularities along with any unwanted spatial QE dependence.

The potential applications of both beam shaping methods presented in this paper are numerous, spanning the many applications of photoelectron sources. For high brightness beam applications, for instance, the transmission of a precise, arbitrary transverse beam shape to the cathode will allow more accurate characterization of the transverse optics during commissioning. While for some applications the laser power required for high current operation may exceed the SLM damage threshold, beam commissioning with high charge and lower duty factor [32] can allow SLM use for injector optimization. Furthermore, the electron feedback method can directly correct for any

quantum efficiency irregularities that arise from photocathode growth or beam operation.

ACKNOWLEDGMENTS

This work was supported by National Science Foundation (Grants No. DMR-0807731 and No. DGE-0707428), as well as the Department of Energy (Grant No. DE-SC00039650).

APPENDIX: DEFORMABLE MIRROR SIMULATIONS AND MEASUREMENT

After the result of [11], in which a deformable mirror was used for transverse laser shaping, we performed both simulations and experiments to characterize the performance of the Okotech 15 mm diameter, 37 actuator deformable mirror. In this micromachined membrane deformable mirror (MMDM), a set of 37 electrodes behind the mirror membrane apply an electrostatic force to the membrane thereby deforming it into programmable shapes. Instead of relying on a genetic algorithm as in [11] to control the shape, which entails using a large number of penalties and figures of merit, we perform modeling of the deformable mirror membrane for a given set of actuator voltages and compare them to experiment.

The shape of the MMDM is described by the Poisson equation:

$$\nabla^2 S(x,y) = \frac{P(x,y)}{T}, \tag{A1}$$

where S is the mirror shape or height, T is the tension in the mirror, and where the electrostatic pressure P is given by

$$P = \frac{\epsilon\epsilon_0 V(x,y)^2}{d(x,y)^2}, \tag{A2}$$

where $d(x,y)$ is the distance between the actuators and the mirror, which is very nearly constant. We will assume it constant in the subsequent analysis. These equations should satisfy boundary conditions with zero deflection at the membrane boundary and beyond. In practice, we then solve an equation of the form

$$\nabla^2 S(x,y) = \beta V_n^2(x,y), \tag{A3}$$

where V_n is a scaled voltage from zero to 1, 1 being the maximum attainable voltage, and β is a constant. The deformable mirror behaves like a perfect concave mirror with adjustable focal length when equal voltages are applied to all actuators, with the focal length scaling linearly with voltage. Measuring the focal length as a function of uniform voltage settings allowed us to determine β. Once we determine the mirror shape for a given set of actuator voltages, then we can simulate the expected output, given a Gaussian input, via full Helmholtz propagation [27,29].

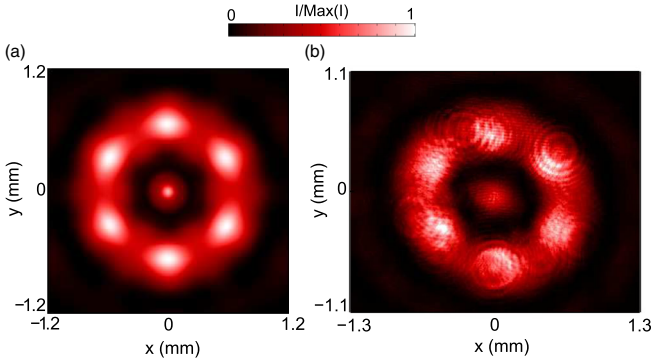

FIG. 10. (a) Simulated laser profile output for setting the MMDM actuator voltages to alternating zero and maximum on each radial hexagonal ring group, using a Gaussian input laser. (b) Experimental output for the conditions simulated in (a).

The 37 mirror actuators are arranged on a hexagonal lattice. This lattice can be viewed as groups of hexagonal rings of actuators about the center actuator. Each actuator is modeled in the 2D solution of Poisson's equation. To test the correspondence of the simulated membrane and the actual mirror, we apply alternating zero and 1 for V_n for each ring of actuators both experimentally and in simulation. The results of both simulation and experimental measurement of this MMDM are shown in Fig. 10. While imperfect, the experimental results agree qualitatively with simulation.

We will now simplify our simulation and assume each set of actuator rings is instead one perfect cylindrically symmetrical ring. This allows us to investigate radial shaping accuracy with an MMDM versus the number of actuators. In this case, the size of each hypothetical actuator ring is modeled after the physical size of the MMDM actuators used above. The behavior of each of these hypothetical MMDMs for an output shape of a 3 mm diameter circular flattop is shown in Fig. 11. Though the

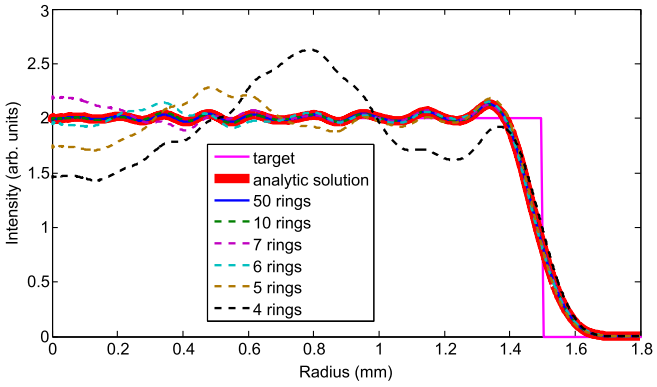

FIG. 11. Simulated output of a 3 mm diameter flattop assuming an ideal MMDM with analytic solution, or assuming the MMDM is composed of varied numbers of perfect actuator rings. The MMDM used in Fig. 10 is four-ring, with each ring being composed of multiple hexagonal actuators.

analytic solution (which corresponds to an ideal MMDM, or infinitely many actuators) does not reproduce the hard edge of the flattop, the flatness of this profile can only be obtained with MMDMs with ten or more rings. The profile given by a four-ring MMDM, which corresponds to the one used above, is far flatter than the input Gaussian, but it has a large error.

We viewed the error inherent in the control of the MMDM membrane as a serious limitation for laser shaping, and chose instead to use an SLM which has the ability to produce a phase profile of higher accuracy. However, for applications where higher errors are tolerable the MMDM may be suitable given its high power rating and its ability to support multiple polarizations. MMDM users may find the above methodology helpful for predicting the output and expected error from an MMDM laser shaping system.

[1] Y. Li, S. Chemerisov, and J. Lewellen, Phys. Rev. ST Accel. Beams **12**, 020702 (2009).

[2] I. V. Bazarov, B. M. Dunham, and C. K. Sinclair, Phys. Rev. Lett. **102**, 104801 (2009).

[3] F. Zhou, A. Brachmann, P. Emma, S. Gilevich, and Z. Huang, Phys. Rev. ST Accel. Beams **15**, 090701 (2012).

[4] O. J. Luiten, S. B. van der Geer, M. J. de Loos, F. B. Kiewiet, and M. J. van der Wiel, Phys. Rev. Lett. **93**, 094802 (2004).

[5] P. Musumeci, J. T. Moody, R. J. England, J. B. Rosenzweig, and T. Tran, Phys. Rev. Lett. **100**, 244801 (2008).

[6] B. J. Claessens, S. B. van der Geer, G. Taban, E. J. D. Vredenbregt, and O. J. Luiten, Phys. Rev. Lett. **95**, 164801 (2005).

[7] A. McCulloch, D. Sheludko, S. Saliba, S. Bell, M. Junker, K. Nugent, and R. Scholten, Nat. Phys. **7**, 785 (2011).

[8] D. Y. Shchegolkov and E. I. Simakov, Phys. Rev. ST Accel. Beams **17**, 041301 (2014).

[9] E. I. Simakov, B. E. Carlsten, and D. Y. Shchegolkov, *AIP Conf. Proc.* ***1507****, 634 (2012).*

[10] J. Grames, P. Adderley, J. Brittian, J. Clark, J. Hansknecht, D. Machie, M. Poelker, E. Pozdeyev, M. Stutzman, and K. Surles-Law, AIP Conf. Proc. **980**, 110 (2008).

[11] F. Matsui, S. Goriki, Y. Shimizu, H. Tomizawa, S. Kawato, and T. Kobayashi, Opt. Rev. **15**, 156 (2008).

[12] R. M. W. van Bijnen, C. Ravensbergen, D. J. Bakker, G. J. Dijk, S. J. J. M. F. Kokkelmans, and E. J. D. Vredenbregt, arXiv:1407.6856.

[13] F. Wyrowski, J. Opt. Soc. Am. A **7**, 961 (1990).

[14] R. Gerchberg and W. Saxton, *Optik (Stuttgart)* ***35****, 237 (1972).*

[15] M. Pasienski and B. DeMarco, Opt. Express **16**, 2176 (2008).

[16] J. A. Davis, D. E. McNamara, D. M. Cottrell, and T. Sonehara, Appl. Opt. **39**, 1549 (2000).

[17] C. Ye, Opt. Eng. **34**, 3031 (1995).

[18] J. Maxson, A. Bartnik, and I. Bazarov, Appl. Phys. Lett. **105**, 171109 (2014).

[19] A. Sharma, T. Tsang, and T. Rao, Phys. Rev. ST Accel. Beams **12**, 033501 (2009).

[20] B. C. Riddick, E. J. Montgomery, R. B. Fiorito, H. D. Zhang, A. G. Shkvarunets, Z. Pan, and S. A. Khan, Phys. Rev. ST Accel. Beams **16**, 062802 (2013).

[21] H. D. Zhang, R. B. Fiorito, A. G. Shkvarunets, R. A. Kishek, and C. P. Welsch, Phys. Rev. ST Accel. Beams **15**, 072803 (2012).

[22] J. Liang, J. R. N. Kohn, M. F. Becker, and D. J. Heinzen, Appl. Opt. **49**, 1323 (2010).

[23] I. Bazarov, D. Ouzounov, B. Dunham, S. Belomestnykh, Y. Li, X. Liu, R. Meller, J. Sikora, C. Sinclair, F. Wise *et al.*, Phys. Rev. ST Accel. Beams **11**, 040702 (2008).

[24] Z. Zhao, A. Bartnik, F. W. Wise, I. V. Bazarov, and B. M. Dunham, Phys. Rev. ST Accel. Beams **17**, 053501 (2014).

[25] LCOS-SLM X10468 series Technical Information 1, Hamamatsu Photonics.

[26] J. Maxson, I. Bazarov, B. Dunham, J. Dobbins, X. Liu, and K. Smolenski, Rev. Sci. Instrum. **85**, 093306 (2014).

[27] F. Dickey and S. Holswade, *Laser Beam Shaping: Theory and Techniques*, Optical Science and Engineering (Taylor & Francis, London, 2000).

[28] B. Kress and P. Meyrueis, *Applied Digital Optics: From Micro-optics to Nanophotonics* (Wiley, New York, 2009).

[29] A. L. Gaunt and Z. Hadzibabic, Sci. Rep. **2**, 721 (2012).

[30] This image was adapted from an official logo of Cornell University. See www.cornellbigred.com or www.cornell.edu.

[31] I. V. Bazarov, A. Kim, M. N. Lakshmanan, and J. M. Maxson, Phys. Rev. ST Accel. Beams **14**, 072001 (2011).

[32] C. Gulliford, A. Bartnik, I. Bazarov, L. Cultrera, J. Dobbins, B. Dunham, F. Gonzalez, S. Karkare, H. Lee, H. Li, Y. Li, X. Liu, J. Maxson, C. Nguyen, K. Smolenski, and Z. Zhao, Phys. Rev. ST Accel. Beams **16**, 073401 (2013).